Inductive Power Transfer System With High Misalignment Based on Detuned Series-Series Compensation Topology

Chen Chen, Chaoqiang Jiang, *Senior Member, IEEE*, Fengshuo Yang, Hao Guo, Yue Liu, and Ben Zhang

***Abstract*—To mitigate the output power fluctuation caused by physical misalignment in the inductive power transfer (IPT) system, a novel discrete frequency detuned method is proposed. Based on series-series (S-S) compensation topology, a general mathematical model considering the imaginary part and equivalent series resistance has been derived. Subsequently, the output power, primary current, and transmission efficiency against mutual inductance under various frequencies are numerically analyzed. A modified transmission model with higher calculation accuracy, considering the inductance change, is proposed. Systematic design procedures and operation principles of detuned S-S IPT systems are presented, which showcase highly flexible design freedom with any output fluctuation requirements. Finally, an IPT system with adjustable working frequencies is built to verify the theoretical analysis. The experimental results show appealing advantages over other methods, with the minimized power fluctuation of 1.63% when the coupling coefficient changes from 0.53 to 0.22. The IPT system realizes 300 W output with a maximum transmission efficiency of 94.9% .**

***Index Terms*—Frequency detuning, inductive power transfer (IPT), misalignment tolerance, power fluctuation.**

I. Introduction

INDUCTIVE power transfer (IPT) presents various advantages and has been regarded as the most effective charging method for uncrewed systems. This novel charging technology has been used in many situations, including drones, autonomous underwater vehicles (AUV), and autonomous guided vehicles (AGV) [1], [2], [3].

Separate coils are employed on the primary and secondary sides, forming a loosely coupled transformer configuration with a low coupling coefficient. In practical scenarios, the receiver (Rx) often does not align properly with the transmitter (Tx), leading to output fluctuations and reduced efficiency. Consequently, ensuring misalignment tolerance and minimizing output fluctuations remain key challenges in IPT systems. To improve the misalignment capability, coupler optimization for creating a wider magnetic field and cascaded modulation circuits for controlling stable output are two traditional solutions [4], [5]. The primary purpose of the first alternative is to widen the effective coupling magnetic field distribution within a large charging area. A novel O-to-OXY compact coupler is proposed to enhance the misalignment ability in both lateral and longitudinal directions. The O coil and XY coil in the receiver are decoupled, presenting over 17% efficiency improvement when offset up to 150 mm [6]. An overlapped coil on the primary side is discussed in [7], which can mitigate the negative impact of the cross-coupling between the adjacent coils. The transmission efficiency remains above 90% , even with a misalignment of up to 10 cm. In addition, a hybrid topology relay with a coil integrated on the secondary side is designed to increase the mutual inductance stability. Two design degrees are introduced to fabricate the equivalent mutual inductance and lessen its fluctuation versus the offset, finally achieving a fluctuation of less than 4.89% [8]. Besides, many control methods have been studied to mitigate output fluctuations, including phase-shift angle, duty cycle control, and pulse density modulation for full bridge inverter and dc-dc converter [9], [10], [11]. These methods mainly change the system input voltage or regulate the output voltage on the secondary side according to detection signals. Reference [12] introduces a novel method for detecting misalignment in a double-sided *LCC* compensation network by analyzing the harmonic spectrum of the primary-side current, eliminating the need for a communication link.

Phase-shift control on the inverter may cause the soft switch to fail and result in a larger loss. Besides, duty cycle control requires a deep modulation under a large offset, leading to instability and failure of regulation [13]. Furthermore, the coil inductance value may slightly change when misalignment happens for the coupler with a magnetic core. Minor variations will also impact transmission efficiency and cause calculation errors [14]. Variable capacitors and inductors on both sides are set to enhance the power transfer ability in weak coupling regions for electric vehicle (EV) charging [15]. However, the introduced components will increase the system's complexity and lead to

Received 12 August 2025; revised 12 November 2025; accepted 9 December 2025. Date of publication 17 December 2025; date of current version 20 March 2026. This work was supported by the Research Grants Council, Hong Kong SAR under Grant YCRG C1002-23Y and Grant C7003-22Y. Recommended for publication by Associate Editor M. Ponce-Silva. *(Corresponding author: Chaoqiang Jiang.)*

Chen Chen, Chaoqiang Jiang, Hao Guo, Yue Liu, and Ben Zhang are with the Department of Electrical Engineering and the State Key Laboratory of Terahertz and Millimeter Waves, City University of Hong Kong, Hong Kong, and also with the City University of Hong Kong Shenzhen Research Institute, Shenzhen 518057, China (e-mail: chen.chen@my.cityu.edu.hk; chjiang@cityu.edu.hk; hguo33-c@my.cityu.edu.hk; yueliu@cityu.edu.hk; zhang.ben@cityu.edu.hk).

Fengshuo Yang is with the School of Electrical Engineering and Automation, Harbin Institute of Technology, Harbin 150001, China (e-mail: fengshuoyang@stu.hit.edu.cn).

Color versions of one or more figures in this article are available at https://doi.org/10.1109/TPEL.2025.3645191.

Digital Object Identifier 10.1109/TPEL.2025.3645191

extra loss. A separate control for the variable capacitor is applied on the primary and secondary sides to eliminate the dual-sided communication. Flexible compensating for the various self-inductances improves transmission efficiency [16]. A clamped rectifier is proposed in [24], which can change the working mode of the secondary rectifier and regulate the equivalent impedance. In this way, the output power fluctuation is able to be minimized by combining two power curves. To achieve stable output power under misalignment conditions, an X-type compensation topology is designed [25]. In contrast to the S-S topology, it is not sensitive to the varying coupling. However, this function is achieved at the cost of system transmission efficiency, and the power fluctuation could be further improved. Through the strategic switching of operating frequencies, the compensation network dynamically reconfigures between a dual-coupled SP-S topology and a detuned S-S topology. Besides, a reconfigurable topology based on the S-S topology is proposed, which can modulate the input impedance, thus realizing the stable output power through a topology switch [27]. Different from the topology design and optimization, a hybrid structure consisting of four bipolar couplers is investigated in [28]. However, the proposed coupler requires many sub-coils and compensation components, increasing the system's complexity and weight. In our previous work, detuned LCC-S and S-S topologies are combined, and the final output power possesses relatively low fluctuation when the coupling coefficient changes from 0.254 to 0.09 [29].

Apart from the above methods, detuning is another alternative to overcome the mentioned defects. Conventionally, a full-resonant case (FRC) has high power transfer ability because of zero reactive power. However, to realize zero-voltage switching (ZVS) for the inverter, a weak inductive state is typically preferred, which could be named as the quasiresonant case (QRC) [17]. QRC is very close to the FRC and is often used to replace the FRC in practical research and applications. However, the detuned case (DTC) discussed in this article is different; it has more resonant deviation than QRC, and the imaginary impedance should be considered when modeling. Few studies focus on DTC, and its systematic modeling and related analysis are still scarce. In [18], the detuned method is used to control the power between the two receiving sides, realizing equitable power distribution. In [19], the detuned capacitor is utilized to decrease the power loss in uncoupled repeater coils for dynamic wireless power transfer systems. Experimental results demonstrate that proper resonant capacitor selection can limit power fluctuation to approximately 8.5% . In [20], an offline parameter-detuned method for EV wireless charging is proposed by changing the value of parallel-compensation capacitors. However, the achievement of variable capacitors requires additional switches and complex control strategies. In addition, fundamental and third harmonic power channels are superimposed to maintain a smooth output power under detuned working frequency [21]. However, the prerequisite condition of constant output power is strong coupling (coupling coefficient ranges from 0.35 to 0.74), which does not match most IPT scenarios. The study in [22] investigates a primary inductively and secondary capacitively tuned system to provide a wide and stable output power region. But the final output power fluctuation is up to 20% , which could be improved further.

This article uses the frequency-detuned method to improve misalignment tolerance and minimize output fluctuation for IPT systems. Based on the S-S compensation topology, a general mathematical transmission model has been derived in detail, considering both the imaginary part of the impedance and the equivalent series resistance (ESR) of coils. The relationship among output power, transmission efficiency, and frequency-detuned coefficients is analyzed theoretically. Different from the resonant cases, maximum output power points exist on the power curves as misalignment happens. Thus, the convex segment near the peak points presents a smoother power change, which provides the possibility for a sectional combination to form a new curve with low power fluctuation. Importantly, the transmission efficiency will not be affected within a range of detuned frequencies. The contributions of this article include the following.

1) This article proposes a general design procedure for a frequency detuned S-S IPT system, which realizes stable output power without dual-sided communication and a complex control strategy.
2) Transmission model of the frequency DTC is deduced, and detailed analyses regarding of maximum output power point position and power value under misalignment conditions are given.
3) A modified model that accounts for coil inductance variation is proposed to enhance calculation accuracy.

The rest of this article is organized as follows. Section II establishes the mathematical model for the detuned IPT system and discusses its transmission performance under various misalignment cases. Then, the detailed design procedures with low power fluctuation for the AUV IPT system are given in Section III. Subsequently, corresponding experiments are taken to verify the theoretical analysis and design procedures. Finally, Section V concludes this article.

II. Frequency-Detuned AUV IPT System and Its Mathematical Model

The diagram of the AUV IPT system is demonstrated in Fig. 1. The AUV has the function of making an auto-power supply according to the state of the battery. If the battery is low, it can decide to search for the nearest charging station and go there for a power supply [23]. The robot arm is used to fix the AUV after it stops on the charging dock. Besides, the AUV can be regarded as a moving battery and supplies power to other AUVs through IPT. In practice, there will be more or less physical misalignment between the primary and secondary sides when it stops on the charging dock, even with a position control assistance system. These offsets may significantly jeopardize the power transmission performance. It should be emphasized that this article focuses on the misalignment issue after it stops on the charging dock, and the misalignment situation discussed is static charging instead of dynamic charging.

The S-S compensation topology is adopted in this article because of its simplest structure, and the circuit model of the frequency-detuned system with misalignments is illustrated in Fig. 2. When the receiver is located at different positions, the

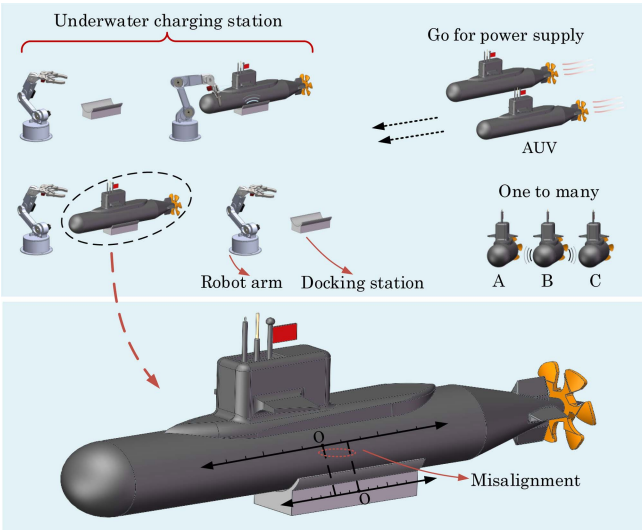

Fig. 1. Diagram of autonomous underwater vehicle IPT charging system and its potential misalignment.

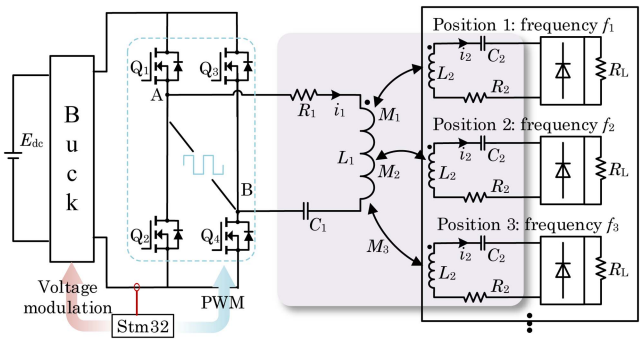

Fig. 2. Structure of frequency-detuned S-S compensation IPT system. Note: It is not a dynamic IPT system, the receiver is immobile; it demonstrates the possible docking position of AUV.

output power can be maintained near the rated level by choosing suitable working modes with specific operating frequencies. Meanwhile, the primary controller will help discretely regulate the input voltage. The system parameters, such as compensation capacitors, are initially designed based on the resonant case. The practical operating frequency is off-resonant, which means the impedance of the inductor and capacitor cannot cancel each other when deriving the mathematical model. Fundamental harmonic approximation and KVL's law are applied. The general transmission model of the frequency-detuned S-S compensation IPT system can be expressed as follows:

$$\begin{bmatrix} U_{\mathrm{AB}} \\ 0 \end{bmatrix} = \begin{bmatrix} j(\omega L_1 - 1/\omega C_1) + R_1 & -j\omega M \\ -j\omega M & j(\omega L_2 - 1/\omega C_2) + R_2 + R_{\mathrm{eq}} \end{bmatrix} \times \begin{bmatrix} I_1 \\ I_2 \end{bmatrix} \tag{1}$$

R_1 and R_2 are the ESR of primary and secondary resonant tanks, respectively. $R_{\mathrm{eq}} = 8R_{\mathrm{L}}/\pi^2$ represents the equivalent ac resistance of the rectifier and load R_{L}. To simplify the model, some substitutions can be set, $X_1 = \omega_1 L_1 - 1/\omega_1 C_1$, $X_2 = \omega_2 L_2 - 1/\omega_2 C_2$, $X_{\mathrm{M}} = \omega M$. The ω_1, and ω_2 represent the angular frequency, and the subscripts "1", and "2" stand for the primary and secondary sides, respectively. In this frequency-detuned IPT system, the working frequency on the primary side and secondary side is the same, $\omega_1 = \omega_2 = 2a\pi f$. The variable $a = f/f_0$ is introduced to describe the detuned degree, namely the detuned coefficient. The f_0 represents the frequency in the FRC, and f represents the practical working frequency. Because of various voltage gains in different DTCs, the bulk module is adopted to regulate the input voltage to keep the maximum power at the same level among the four cases.

From (1), the current in the primary and secondary resonant tanks could be expressed as follows:

$$I_1 = \frac{jX_M U_{\mathrm{AB}}}{-X_1 X_2 + jX_1\lambda + jX_2 R_1 + R_1\lambda + {X_M}^2} \tag{2}$$

$$I_2 = \frac{U_{\mathrm{AB}}(jX_2 + \lambda)}{-X_1 X_2 + jX_1\lambda + jX_2 R_1 + R_1\lambda + {X_M}^2} \tag{3}$$

where $\lambda = R_2 + R_{\mathrm{eq}}$, the expressions of I_1 and I_2 contain complex parts. Substitutions could be taken further to simplify (2) and (3).

$$\begin{cases} \delta = \lambda X_1 + X_2 R_1 \\ \gamma = {X_M}^2 - X_1 X_2 + \lambda R_1. \end{cases} \tag{4}$$

Therefore, I_1 and I_2 could be rewritten as follows:

$$I_1 = U_{\mathrm{AB}} \frac{\delta X_2 + \lambda\gamma + j(\gamma X_2 - \delta\lambda)}{\delta^2 + \gamma^2} \tag{5}$$

$$I_2 = U_{\mathrm{AB}} X_M \frac{\delta + j\gamma}{\delta^2 + \gamma^2}. \tag{6}$$

The imaginary and real parts of the I_1 can be calculated as follows:

$$\begin{cases} \mathrm{Im}(I_1) = U_{\mathrm{AB}} X_2 \frac{j(\gamma+\delta)}{\delta^2+\gamma^2} \\ \mathrm{Re}(I_1) = U_{\mathrm{AB}} \lambda \frac{j(\gamma-\delta)}{\delta^2+\gamma^2}. \end{cases} \tag{7}$$

Besides, the voltage gain can be expressed as follows:

$$G_v = \frac{X_M R_{\mathrm{eq}}}{\sqrt{\delta^2 + \gamma^2}}. \tag{8}$$

Then, the input power P_{in} and output power P_{o} can be derived as follows:

$$P_{\mathrm{in}} = \frac{U_{\mathrm{AB}}(\lambda\gamma + \delta X)}{\delta^2 + \gamma^2}, \quad P_o = \frac{(U_{\mathrm{AB}} X_M)^2 R_{\mathrm{eq}}}{\delta^2 + \gamma^2}. \tag{9}$$

Thus, the general expression of transmission efficiency can be given as follows:

$$\eta = \frac{X_M^2 R_{\mathrm{eq}}}{\lambda\gamma + \delta X_2}. \tag{10}$$

In traditional resonant cases, X_1 and X_2 are usually assigned as "0." Substitute the special condition $X_1 = X_2 = 0$ into (10), and the obtained transmission efficiency formulation is consistent with existing literature, thereby offering the preliminary verification of the derived mathematical model.

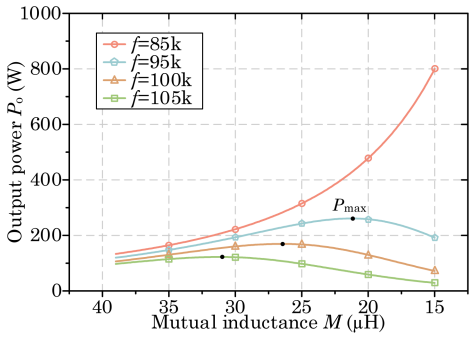

Fig. 3. Simulated output power P_o under different mutual inductances in resonant and DTCs.

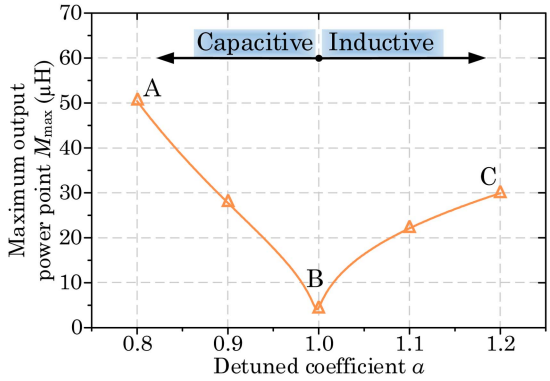

Fig. 4. Maximum output power point versus the detuned coefficient.

From (4) and (9), the output power under the detuned situation can be calculated as follows:

$$P_o = \frac{U_{AB} R_{eq}\, \omega^2}{M^{-2}\left((\omega^2 M^2 + \lambda R_1 - X_1 X_2)^2 + \left(\lambda X_1 + X_2 R_1\right)^2\right)}. \tag{11}$$

Equation (11) demonstrates that the output power is the function of mutual inductance M and operating angular frequency ω (detuned coefficient a in essence). To investigate the relationship among P_o and M, ω, P_o can be rewritten as follows:

$$P(M,\omega) = \frac{U_{AB} R_{eq}}{\omega^2}\left(\frac{e^2+\delta^2}{M^2} + \omega^4 M^2 + 2\omega^2 e\right)^{-1} \tag{12}$$

where $e = \lambda R_1$-$X_1 X_2$. From (12), it can be noticed that output power will increase first and then decrease as mutual inductance M increases on the condition of a fixed angular frequency.

Then, a partial derivative of the variable M can be given as follows:

$$\frac{\partial P}{\partial M} = \omega^4 M - (e^2 + \lambda X_1 + X_2 R_1) M^{-3} \tag{13}$$

by taking $\partial P/\partial M = 0$, the expression of the maximum mutual inductance point M_{max} is yielded when the output power reaches the peak point.

$$M_{max} = \frac{\sqrt[4]{e^2 + (\lambda X_1 + X_2 R_1)^2}}{2\alpha\pi f}. \tag{14}$$

III. Design for the Detuned System With Low Output Power Fluctuation

A. Output Power Characteristics Versus Coefficient a

Based on the above theoretical analysis, (14) indicates that the maximum output power point is a function of the detuned coefficient a. The coefficient a determines the location of the maximum output power point, a critical parameter in detuned IPT system design.

Fig. 3 illustrates the simulated output power P_{out} in resonant and detuned situations when the mutual inductance changes from 39 μH to 15 μH. The 85 kHz represents the FRC, and the other three have certain frequency deviations, namely, DTC cases. As shown in Fig. 3, the output power increases rapidly as M decreases in FRC. In contrast, the maximum output power points exist on the power curves of DTC, and the position of P_{max} will move close to the full alignment position as the detuned frequency increases. These simulation results are in accordance with the theoretical analysis.

Fig. 4 demonstrates the relationship between the detuned coefficient and the value of mutual inductance when the output power reaches the peak point. As shown in Fig. 4, the M_{max} decreases first as a changes from X_A to X_B, then begins to climb as a changes from X_B to X_C. Usually, the IPT system tends to operate in the inductive resonant state (BC interval) to achieve ZVS operation. In the BC interval, the M_{max} has an increasing tendency with the increment of a. In other words, the location of the maximum output point will move toward the full alignment position as a increases, which corresponds to the pattern shown by the power curves in Fig. 3. In addition, the changing rate of the M_{max} is larger in the capacitive state than that of the inductive state, revealing that the position of maximum output power point is more sensitive to the misalignment under capacitive situations.

B. Transmission Efficiency

Another design consideration is transmission efficiency. Similarly, based on (4) and (10), the transmission efficiency can be derived as follows:

$$\eta = R_{eq}\left(\lambda + \frac{\lambda^2 R_1 + {X_2}^2 R_1}{\omega^2 M^2}\right)^{-1}. \tag{15}$$

Equation (15) demonstrates that the transmission efficiency is the function of mutual inductance M and operating angular frequency ω (detuned coefficient a in essence). To investigate the relationship among η, M, and ω, the denominator of (15) could be rewritten as follows:

$$\eta(M,\omega) = \frac{R_1}{M^2}\left[\frac{1}{\omega^4 {C_2}^2} + \frac{1}{\omega^2}\left(\lambda^2 - \frac{2L_2}{C_2}\right) + {L_2}^2\right] + \lambda. \tag{16}$$

From (16), it can be roughly found that under constant mutual inductance M, the transmission efficiency initially increases with angular frequency ω before reaching a maximum and subsequently decreases.

A partial derivative of the variable ω is taken as follows:

$$\frac{\partial \eta}{\partial \omega} = \frac{2R_1}{M^2}\left(-\frac{\lambda^2}{\omega^3} + \frac{2L_2}{C_2\omega^3} - \frac{2}{{C_2}^2\omega^5}\right). \tag{17}$$

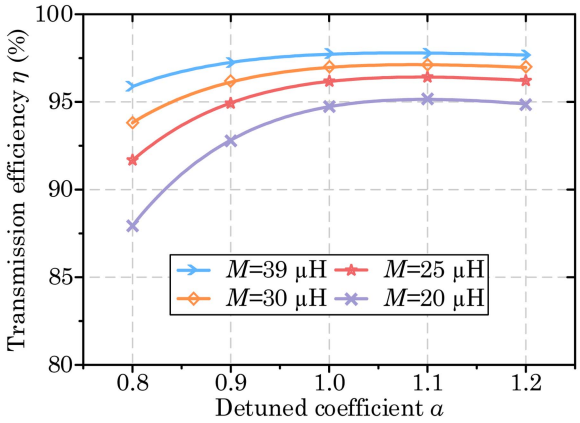

Fig. 5. Transmission efficiency versus operating frequency with various mutual inductances.

By setting $\partial\eta/\partial\omega = 0$, the solution of the angular frequency point $\omega_{\max}$ can be obtained when the transmission efficiency is maximum.

$$\omega_{\max} = 2\alpha\pi f = \frac{1}{2\pi}\sqrt{\frac{2}{C_2\left(2L_2 - C_2\lambda^2\right)}}. \tag{18}$$

Equation (18) indicates that the maximum efficiency point $\omega_{\max}$ is a fixed value when the IPT system is determined, mainly depending on the secondary coil inductance L_2, compensation capacitor C_2, and load R_{L}.

The Fig. 5 demonstrates the transmission efficiency versus the detuned coefficient under different misalignment cases. It can be found that the transmission efficiency will decrease as the mutual inductance reduces from 39 μH to 20 μH. When the mutual inductance is fixed, the transmission efficiency has no obvious difference when α changes from 1.0 to 1.2. The discrepancy is larger in the capacitive region than in the inductive region. Therefore, changing the operating frequency in a narrow range is allowable in terms of transmission efficiency.

C. Design for Lowering Output Fluctuation

As mentioned in the last section, the maximum output power points exist on the power curve when the frequency deviates from the resonant one, and the top region near the peak point has a flatter change with lower fluctuation. Therefore, the top areas on the power curve with different detuned coefficients can be combined to form the final output power curve. As shown in Fig. 6(a), three power curves in the DTCs are presented. The final power curve is highlighted in a darker color, combined with the three top segments, and the square-shaded area illustrates the effective working region. The power fluctuation can be calculated as follows:

$$F = \frac{P_{\max} - \min\{P_1, P_2, P_3, P_4\}}{P_{\max} + \min\{P_1, P_2, P_3, P_4\}} \tag{19}$$

where the $P_{\max}$ is the rated output power, and P_2, P_3 are the power values of the intersection points, and P_1, P_4 represent the power values of the start and end points. The interval between P_1 and P_4 is the effective operation region. The design goal is to

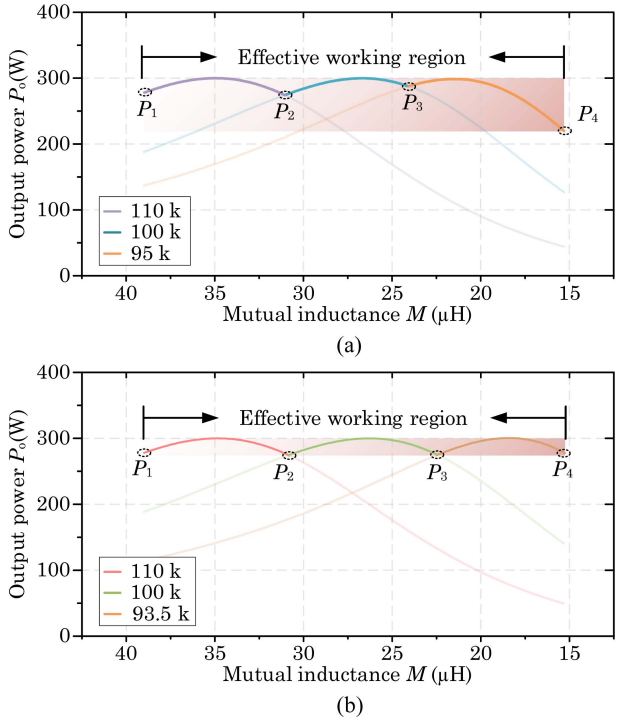

Fig. 6. Combined output power of detuned IPT systems. (a) Without optimization. (b) Ideal power curve with lower fluctuation.

minimize the power fluctuation F, which is mainly determined by the lowest value of P_1, P_2, P_3, and P_4 because the $P_{\max}$ is usually fixed and known.

As illustrated in Fig. 6(a), the lowest power point is P_4; thus, the power fluctuation could be calculated as follows:

$$F_1 = \frac{P_{\max} - P_4}{P_{\max} + P_4}. \tag{20}$$

It is obvious that the calculated F_1 is not the optimal solution because the value of P_4 aggravates the power fluctuation, while the values of P_1, P_2, and P_3 are closer to the rated power than that of P_4. The optimal case is that the value of these points can be maintained the same and reach a relatively high level, which can be achieved by setting the detuned coefficient. The ideal output power curve with lower fluctuation is plotted in Fig. 6(b). The power values of the intersection points are kept consistent with the start and end points. In this way, the output power fluctuation can be minimized, and the optimal design can be realized. The flow chart of the design procedures is demonstrated in Fig. 7. For the concrete IPT system, the coil inductance and mutual inductance could be measured in advance. The compensation capacitors are designed based on the resonant case. According to the design requirement, the minimum allowable power value can be calculated by (19) because the rated power and power fluctuation are provided in advance. As analyzed in the above section, to realize the optimal design, the minimum power value should be the same as the power value of the start point P_1. The mutual inductance of the coupler versus the misalignment can also be measured, including the start and end points (M_1 and M_{n}). Therefore, the detuned coefficient α_1 can be calculated by

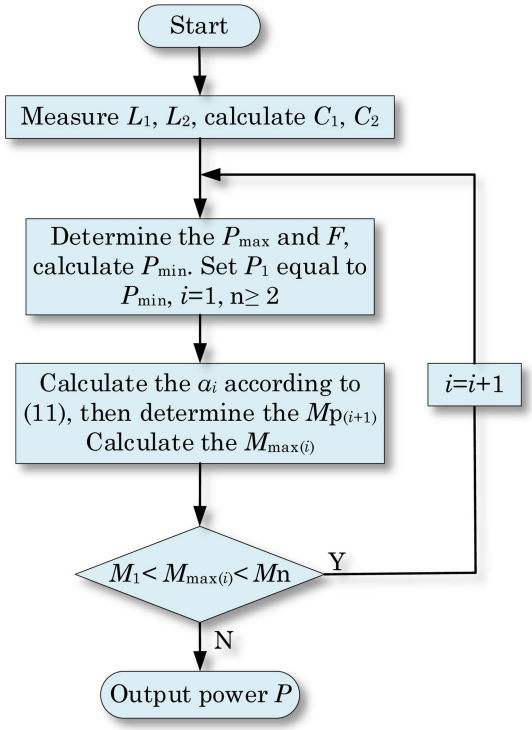

Fig. 7. Flow chart of the design procedures for the detuned IPT system.

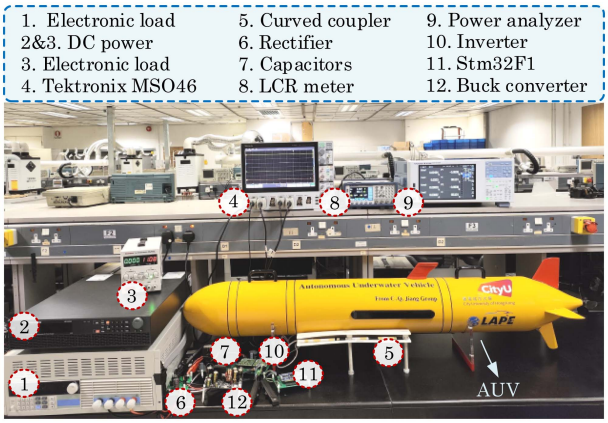

Fig. 8. Experiment platform of AUV IPT system with frequency detuned S-S compensation topology.

(11), then the corresponding point with the same power value on the power curve after the peak point can be determined. Thus, take this point as the start point for the next power curve. Until the calculated $M_{max(i)}$ is beyond the range of mutual inductance within the effective working region, the design procedure ends. It should be noted that to achieve low-power fluctuation, more combined power curve sections are needed.

IV. Experiment Verification

A. Transmission Characteristics

To verify the proposed method for mitigating the output power fluctuation, a 300 W experiment platform with a curved coupler for AUV is fabricated, as shown in Fig. 8. The full-bridge inverter consists of two half bridges of EPC9099, and the PWM signals

TABLE I
Parameters of the Detuned SS IPT System

Symbol	Quantity	Value
L_1	Inductance of the primary coil	73.95 μH
L_2	Inductance of the secondary coil	72.05 μH
C_1	Compensated capacitor	47.6 nF
C_2	Compensated capacitor	49.26 nF
f_0	Initial resonant frequency	85 kHz
f	Operation frequency	93.5–110 kHz
P	Rated output power	300 W

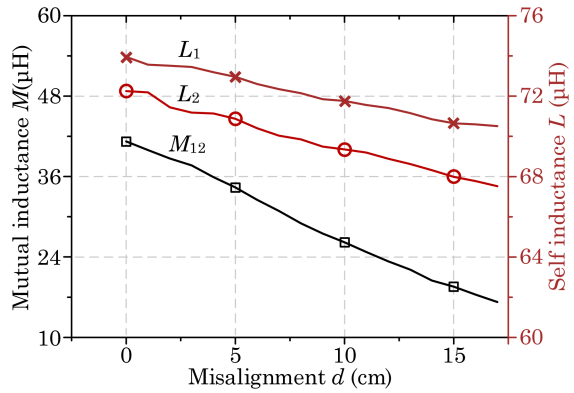

Fig. 9. Inductance of primary and secondary coil and mutual inductance versus the misalignment.

with controllable frequencies are generated by STM32F103. A current sensor is set on the primary dc side, providing the feedback for power curve selection. The Tektronix oscilloscope MSO46 is used for acquiring input and output waveforms. Besides, the power analyzer WT5000 is utilized for power and efficiency measurement. Detailed experimental parameters are tabulated in Table I.

The measured self-inductance and mutual inductance versus the misalignment are plotted in Fig. 9. It can be found that as the misalignment increases, the mutual inductance has a decreasing trend, which is in line with common sense. The self-inductance of the primary and secondary coils has a slight discrepancy because of the manual wound, but the tiny error is acceptable. The value of the self-inductance will drop as the misalignment increases due to the existence of magnetic material. This deviation has been neglected in most research for simplification. The value of ΔL_1 and ΔL_2 reaches 3.44 μH and 4.73 μH, respectively, when the misalignment changes from 0 cm to 17 cm.

The combined output power is plotted in Fig. 10, highlighted by the four short bold lines. The light-colored lines are the original power curves before the combination. As can be seen, the maximum power reaches 300 W, and the lowest power is around 290 W; thus, the power fluctuation is merely 1.7% . It should be noted that the power fluctuation is adjustable according to the design requirement. If a smaller power fluctuation is required, more segments of the top regions of the power curve with different detuned coefficients are needed. However, for the AUV-IPT system discussed in this article, four top segments from different

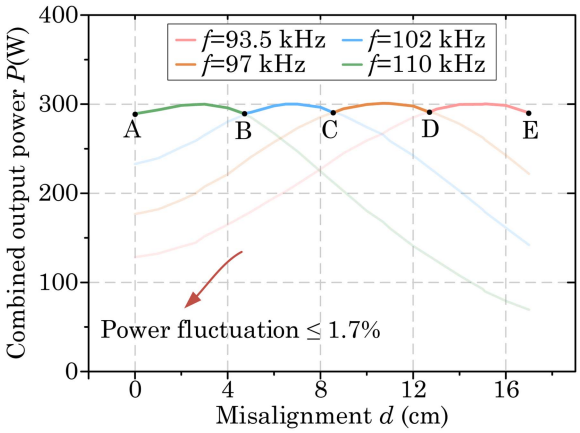

Fig. 10. Combined output power with fluctuation is less than 1.7% .

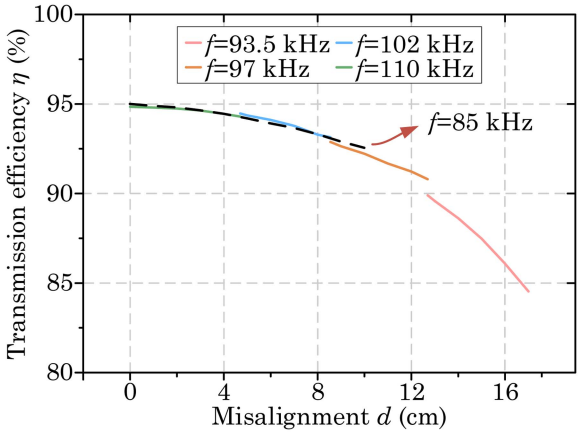

Fig. 11. Transmission efficiency of detuned and resonant cases versus the misalignment.

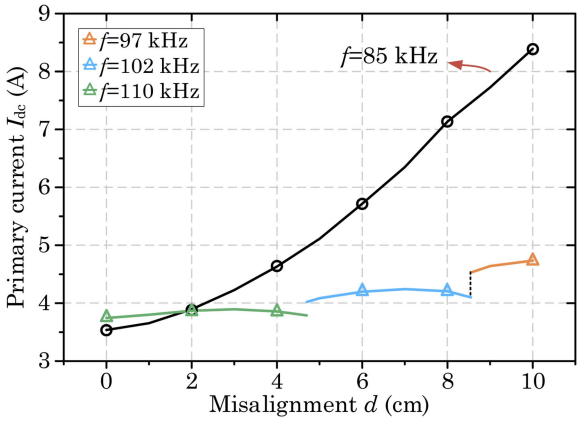

Fig. 12. Primary current comparison between detuned and resonant cases under misalignment.

power curves are enough to minimize the output power under an extensive misalignment range. The experiment results show that the proposed method can effectively reduce the output power fluctuation without relying on a complex control strategy.

The transmission efficiency of the proposed detuned IPT AUV system under different misalignments is illustrated in Fig. 11. Fig. 12 plots the primary dc current in the resonant and DTCs

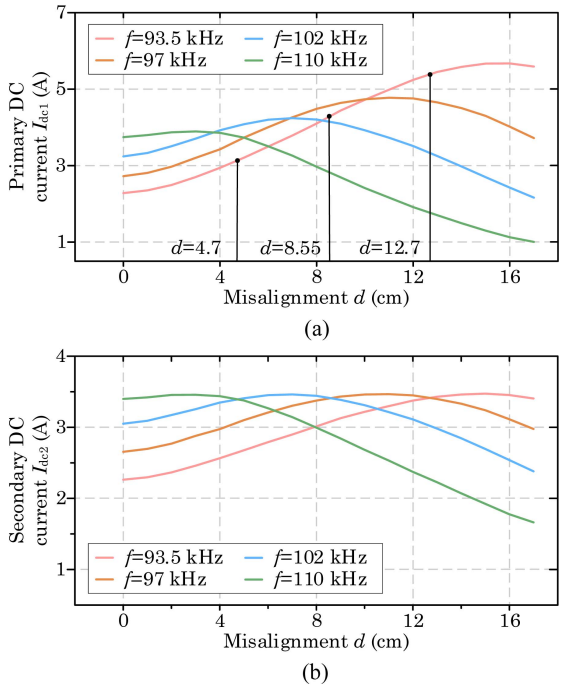

Fig. 13. DC current in the primary and secondary sides versus the misalignment. (a) Primary current. (b) Secondary current.

versus the misalignment. When the misalignment comes to 10 cm, the primary current is over 8.4 A. Thus, the experiment is terminated to avoid the current surge breaking the system. The maximum dc current in the DTC is only 4.7 A, which means the current surge can be mitigated, and more misalignment is allowable. Compared with the resonant case (85 kHz), the final transmission efficiency does not have much attenuation. Therefore, frequency deviation in a certain range is acceptable.

B. Charging Mode Selection Strategy

Fig. 13 illustrates the dc current in the primary and secondary sides under DTCs (93.5, 97, 102, and 110 kHz). As with the output power, the secondary dc current I_{dc2} has a similar changing tendency to the constant load used in the experiment. Although peak points exist in the curves of primary side dc current, the amplitude varies due to different input impedances among these cases. The output can be divided into four parts according to the intersection points on the power curve. Therefore, the frequency and voltage modulation can also be determined by these points according to (11). The secondary side dc current can be detected by the current sensor and utilized as the charging mode selection criterion. The current range is set as 3.405–3.464 A, corresponding to the output power of 300 W. However, communication between the two sides is needed, which will increase the system's complexity and reduce its robustness. Similarly, the primary side dc current can also be used to choose a mode. It should be emphasized that only the current curve with a monotonic changing tendency (93.5 kHz and 110 kHz) is suitable for taking as the judgment criteria. The reason is that using the current curve with a monotonic change will lead to a misjudgment. Besides, the current in the case of 93.5 kHz is smaller than in other cases (The misalignment usually tends to light offset

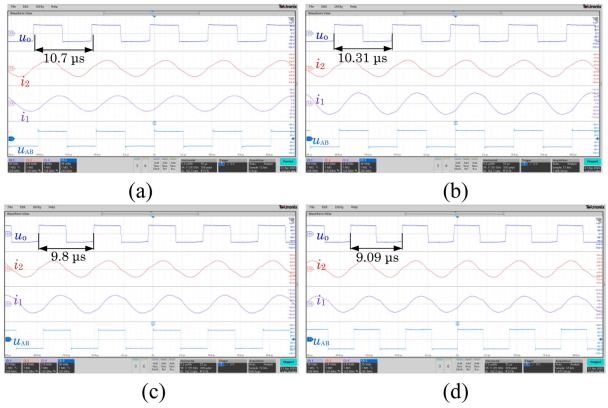

Fig. 14. Measured waveforms of u_{AB}, i_1, u_o, i_2 when output power is 300 W in four detuned situations. (a) $f = 93.5$ kHz. (b) $f = 97$ kHz. (c) $f = 102$ kHz. (d) $f = 110$ kHz.

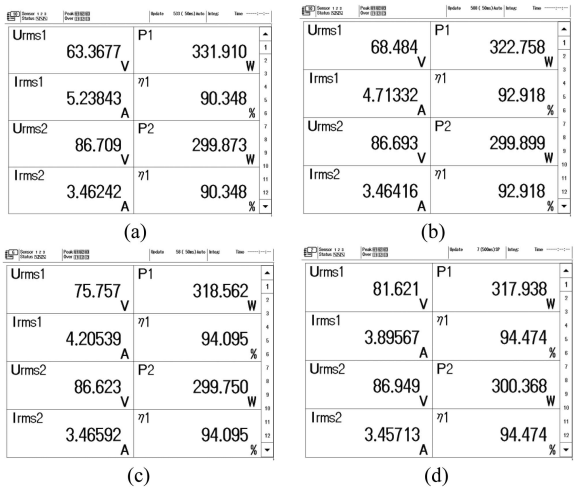

Fig. 15. Measured transmission efficiency in four DTCs when output power reaches 300 W. (a) $f = 93.5$ kHz. (b) $f = 97$ kHz. (c) $f = 102$ kHz. (d) $f = 110$ kHz.

instead of heavy offset). Therefore, the current of the case with 93.5 kHz is taken as the basis for choosing the mode.

When an AUV stops on the charging dock with a certain misalignment, the primary dc current is detected, and the STM32 microcontroller will change the working frequency based on that current value. Concretely, a primary current between 2.28–3.15 A, indicating a 0–4.7 cm misalignment, triggers a 110 kHz operating frequency, while a current between 3.15–4.32 A, corresponding to a 4.7–8.55 cm misalignment, shifts the frequency to 102 kHz.

In addition, the current and voltage waveforms of the input and output sides in four cases are captured in Fig. 14. The presented working frequencies are in accordance with the design. Four cases exhibit inductive input impedance and meet the ZVS condition, as confirmed by the phase difference between voltage and current waveforms. The screenshots of transmission efficiency in the four DTCs when output power reaches 300 W are

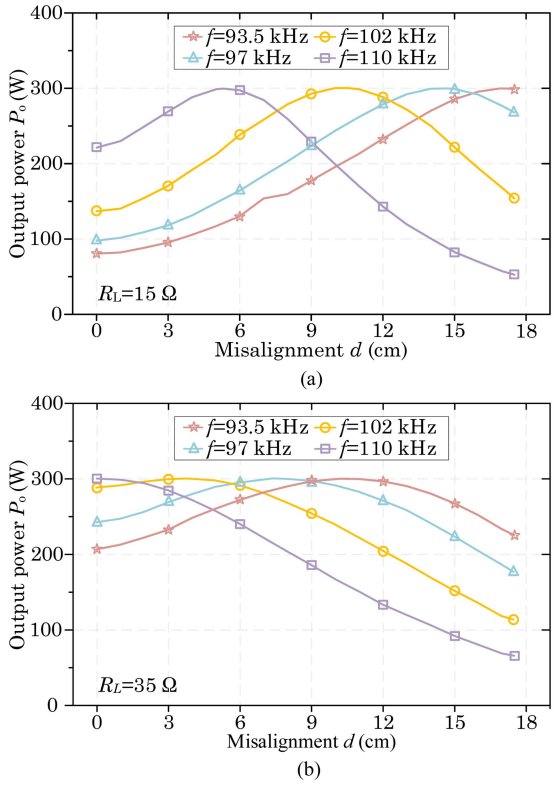

Fig. 16. Output power curves versus misalignment at different loads. (a) $R_L = 15\ \Omega$. (b) $R_L = 35\ \Omega$.

demonstrated in Fig. 15. Within the effective working region, the system dc transmission efficiency is over 90% , even though the misalignment distance is 15.1 cm. Besides, Fig. 16 demonstrates the output power versus the misalignment at different loads. It can be found that the position of the maximum power points will move to the position of full alignment as the load increases. In addition, when the load is fixed, the P_{max} will also move to the full alignment position as the detuned frequency increases.

C. Modified Transmission Model

From the experiment, the inductance of the primary and secondary coils will change as the misalignment happens. In this article, these changes are considered to accurately establish the transmission model for the detuned IPT system. Therefore, a modified transmission model considering the various inductances is given. The expression of the inductance versus misalignment can be obtained by curve fitting.

$$\begin{cases} L_1(d) = -0.2116d + 73.914 \\ L_2(d) = -0.2767d + 72.158 \\ M(d) = -1.4705d + 39.385. \end{cases} \tag{21}$$

Therefore, the modified output power can be rewritten as follows:

$$P_o(d) = \frac{U_{AB} R_{eq} \omega^2 M^2}{\left(\omega^2 M^2(d) + \lambda R_1 - X_1(d) X_2(d)\right)^2 + \left(\lambda X_1(d) + X_2(d) R_1\right)^2}. \tag{22}$$

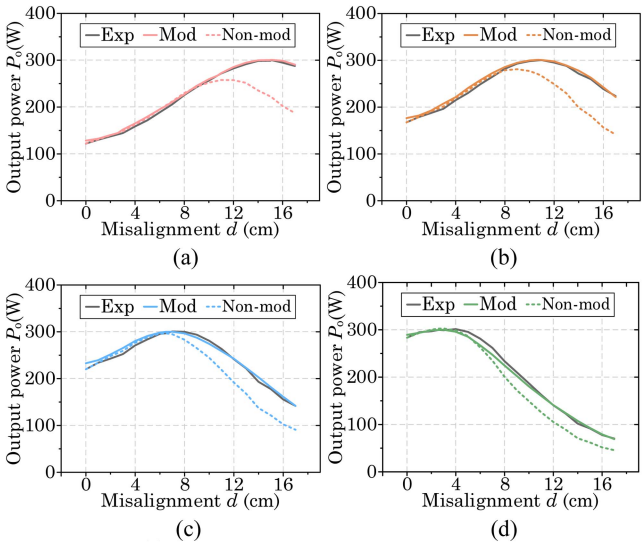

Fig. 17. Modified output power versus the misalignment considering the various inductance values. (a) $f = 93.5$ kHz. (b) $f = 97$ kHz. (c) $f = 102$ kHz. (d) $f = 110$ kHz.

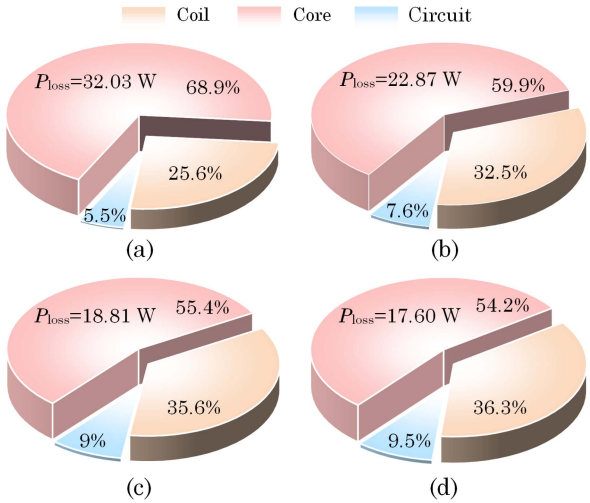

Fig. 18. Loss breakdown of the system in four DTCs when output power reaches 300 W. (a) $f = 93.5$ kHz. (b) $f = 97$ kHz. (c) $f = 102$ kHz. (d) $f = 110$ kHz.

Fig. 17 demonstrates the comparison of output power versus the misalignment obtained by the modified and nonmodified transmission model. The black line represents the experimental measurement results, the dotted line stands for the case of the nonmodified model, and the remaining curve displays the result from the modified model. The results of the modified model are more consistent with the experiment, especially in the large misalignment situation, which verifies the correctness of the proposed modified model.

D. Loss Breakdown

Then, the calculated loss breakdown in four cases when output power reaches 300 W is illustrated in Fig. 18. It can be found that the case at 93.5 kHz shows the highest total loss of 32.03 W, resulting from an offset distance of 15.1 cm and a relatively large current flow. Besides, the loss in the magnetic core occupies most of the total loss, and it has a declining tendency when the frequency increases because the current flow through the primary coil reduces. A large current will bring more core loss. Even if the percentage value of the circuit loss, including the inverter and rectifier, climbs slightly, the calculated circuit loss presents a downward trend because of the reduced primary current from 93.5 kHz to 110 kHz.

E. Comparison With Other Works and Discussion

Many works focus on solutions to improve misalignment tolerance, and a detailed comparison in terms of system complexity, misalignment tolerance, and transmission efficiency is illustrated in Table II. Among these existing methods, the power fluctuation in our work is the lowest, at only 1.63% . Meanwhile, the number of components, including inductors, capacitors, and switches, in our method is also the minimum, which proves the proposed system has the simplest structure. Xiong et al. [26] exhibited the largest misalignment tolerance because the optimization of the overlapping double D coupler is adopted, which inherently has better flux coupling ability. But it possesses most of the components due to the application of hybrid topology. Our work showcases better offset tolerance than [25], [28], and [30]. Besides, the transmission efficiency in [24], [26], [30], and this work can reach up to over 94% . In addition, the detuned SS compensation topology proposed in [30] is similar to the method discussed in this article. The nonmonotone cases (P_{out} versus M) are used to combine the final output power curve. In fact, there are two suitable curves with the same maximum output power. In the proposed method, there are three design freedoms, including the rated output power, and the power fluctuation can be flexibly adjusted according to the requirement. When these two parameters are fixed, the lowest power value can also be calculated. Owing to the multicurve combination, the misalignment range can be extended as the number of curve segments increases.

The frequency detuned method proposed in our work can also be applied in other topologies and scenarios. The key idea of this method is to find the maximum output power points under a detuned situation, and the position of this point is located within the allowable misalignment range. The region around the peak points possesses relatively smaller change tendency, which can be utilized to form the new output power curve with low fluctuation. In addition, this method is to mitigate the charging power fluctuation after the device stops on the charging platform, such as AUVs, AGVs, and drones. Even though the guided technology is used to assist the alignment between the primary and secondary sides, there still exists certain misalignment due to water flow, air flow. While the theoretical analysis and transmission model derived use an AUV as a specific example, the model itself is formulated in a general format, making it applicable to other scenarios for solving similar offset problems. What needs to be adjusted are the system parameters, such as coil inductance, mutual inductance, rated power, and allowable misalignment. These can be measured and substituted into the existing design

TABLE II
COMPARISON WITH EXISTING METHODS

Reference	L+C+S	Frequency (kHz)	Coupling coefficient	Misalignment tolerance	Rated output power (W)	Efficiency	Fluctuation
[24]	2+2+1	200	0.1–0.4	N/A	400	86.1%–94.3%	3.08%
[25]	2+2+0	200	0.14–0.28	4.5/11 cm (40.91%)	100	83.5%–87.5%	9.60%
[26]	6+5+0	85 133. 96	0.1–0.25	32/40 cm (80%)	500	85.37%–94.51%	5%
[27]	2+2+1	250	0.1–0.4	N/A	400	85.8%–91.7%	9.59%
[28]	5+5+0	85	0.26–0.285	22.5/45 cm (44.44%)	3000	87.15%–91.29%	8.00%
[29]	3+4+3	100	0.09–0.254	19/30 cm (63.33%)	200	81.3%–88.12%	2.96%
[30]	2+2+0	236, 257	0.115–0.27	7.2/30 cm (24%)	750	91.46%–95.52%	5.6%
This article	2+2+0	93.5, 97 102, 110	0.22–0.53	17/35 cm (48.57%)	300	87.6%–94.9%	1.63%

procedures and formulas to obtain a new output power curve with low fluctuation.

V. CONCLUSION

This article proposes a frequency-detune method to improve misalignment tolerance for IPT systems. A general mathematical model based on the S-S compensation topology is derived to assist the theoretical analysis. Different from the resonant case, the current surge against the weak coupling can be significantly suppressed, reducing the threat of system breakdown. The primary current reaches 8.39 A when misalignment is 10 cm in the resonant case, while it is only 4.73 A in the proposed system. Considering the various inductance values caused by misalignment, the modified transmission model demonstrates an improvement of over 83% in calculation accuracy. Discrete input voltage modulation range from 59.3 V to 81.4 V could realize the rated output power under misalignment from 0 to 17 cm, presenting a 48.46% improvement compared with FRC. The experiment results demonstrate that the final output curve maintains a rated power of 300 W with a low fluctuation of 1.63% .

REFERENCES

[1] V.-B. Vu et al., "Operation of inductive charging systems under misalignment conditions: A review for electric vehicles," *IEEE Trans. Transp. Electrific.*, vol. 9, no. 1, pp. 1857–1887, Mar. 2023.

[2] C. Chen, C. Q. Jiang, X. Wang, L. Mo, W. Guo, and S. Ren, "Terrace-shaped core design method for inductive power transfer system considering uniform magnetic flux distribution," *IEEE Trans. Ind. Electron.*, vol. 72, no. 8, pp. 7795–7806, Aug. 2025.

[3] Y. Gu, J. Wang, Z. Liang, and Z. Zhang, "Flexible constant-power range extension of self-oscillating system for wireless in-flight charging of drones," *IEEE Trans. Power Electron.*, vol. 39, no. 11, pp. 15342–15355, Nov. 2024.

[4] X. He et al., "A misalignment-tolerant coil array for high output stability and low magnetic field exposure in EV wireless charging system," *IEEE Trans. Ind. Electron.*, vol. 72, no. 10, pp. 10279–10289, Oct. 2025.

[5] C. Cai et al., "Robust wide-area wireless charging of multipath movable receivers: A coupling mechanism and simplified configuration strategy," *IEEE Trans. Power Electron.*, vol. 40, no. 1, pp. 2527–2541, Jan. 2025.

[6] X. Duan, W. Han, Y. Hu, H. Tian, and J. Huang, "2-D misalignment-tolerant wireless power transfer with a compact O-to-OXY magnetic coupler," *IEEE J. Emerg. Sel. Topics Ind. Electron.*, vol. 6, no. 1, pp. 9–18, Jan. 2025.

[7] J. Yin, S. Mekhilef, P. Darvish, H. Mokhlis, and T. K. Soon, "A new cross-overlapped decoupling coil structure for EV dynamic inductive wireless charging system," *IEEE Trans. Ind. Electron.*, vol. 72, no. 2, pp. 1314–1324, Feb. 2025.

[8] Y. Zhang, G. Wei, J. Zhang, L. Hao, and L. Cheng, "A hybrid topology relay based wireless power transfer system with mutual inductance enhancement and high misalignment tolerance," *IEEE Trans. Power Electron.*, vol. 40, no. 6, pp. 7640–7645, Jun. 2025.

[9] J. Liu, F. Xu, C. Sun, and K. H. Loo, "A compact single-phase AC–DC wireless power transfer converter with active power factor correction," *IEEE Trans. Ind. Electron.*, vol. 70, no. 4, pp. 3685–3696, Apr. 2023.

[10] G. Zhu, J. Dong, W. Shi, T. B. Soeiro, J. Xu, and P. Bauer, "A mode-switching-based phase shift control for optimized efficiency and wide ZVS operations in wireless power transfer systems," *IEEE Trans. Power Electron.*, vol. 38, no. 4, pp. 5561–5575, Apr. 2023.

[11] A. T. L. Lee, W. Jin, S.-C. Tan, and S. Y. Hui, "Buck-boost single-inductor multiple-output high-frequency inverters for medium-power wireless power transfer," *IEEE Trans. Power Electron.*, vol. 34, no. 4, pp. 3457–3473, Apr. 2019.

[12] M. Rastegar, M. H. Ghaderi, M. Bahrami-Fard, J. M. Miller, P. T. Balsara, and B. Fahimi, "A self-tuning algorithm for misalignment detection and efficiency optimization in double-sided *LCC* -based DWPT systems," *IEEE Trans. Transp. Electrific.*, vol. 11, no. 5, pp. 11658–11671, Oct. 2025.

[13] J. Luo et al., "Novel cuk-based bridgeless rectifier of wireless power transfer system with wide power modulation range and low current ripple," *IEEE Trans. Ind. Electron.*, vol. 69, no. 3, pp. 2533–2544, Mar. 2022.

[14] H. Zhang, Y. Chen, D.-H. Kim, Z. Li, M. Zhang, and G. Li, "Variable inductor control for misalignment tolerance and constant current/voltage charging in inductive power transfer system," *IEEE J. Emerg. Sel. Topics Power Electron.*, vol. 11, no. 4, pp. 4563–4573, Aug. 2023.

[15] K. Song et al., "A control strategy for wireless EV charging system to improve weak coupling output based on variable inductor and capacitor," *IEEE Trans. Power Electron.*, vol. 37, no. 10, pp. 12853–12864, Oct. 2022.

[16] R. Matsumoto, T. Fujita, and H. Fujimoto, "Communicationless reactance compensation using PWM-controlled switched capacitors for wireless power transfer," *IEEE Trans. Power Electron.*, vol. 38, no. 10, pp. 13194–13206, Oct. 2023.
[17] B. Zhang, C. Q. Jiang, F. Yang, C. Chen, Y. Lu, and J. Zhou, "An antirotation wireless power transfer system with a flexible magnetic coupler for autonomous underwater vehicles," *IEEE Trans. Power Electron.*, vol. 40, no. 1, pp. 2593–2603, Jan. 2025.
[18] N. Desai, C. Juvekar, S. Chandak, and A. P. Chandrakasan, "An actively detuned wireless power receiver with public key cryptographic authentication and dynamic power allocation," *IEEE J. Solid-State Circuits*, vol. 53, no. 1, pp. 236–246, Jan. 2018.
[19] W. Xiong, Q. Yu, Z. Liu, L. Zhao, Q. Zhu, and M. Su, "A detuning-repeater-based dynamic wireless charging system with quasi-constant output power and reduced inverter count," *IEEE Trans. Power Electron.*, vol. 38, no. 1, pp. 1336–1347, Jan. 2023.
[20] J. Deng et al., "Frequency and parameter combined tuning method of LCC–LCC compensated resonant converter with wide coupling variation for EV wireless charger," *IEEE J. Emerg. Sel. Topics Power Electron.*, vol. 10, no. 1, pp. 956–968, Feb. 2022.
[21] W. Xiong et al., "A dual-frequency-detuning method for improving the coupling tolerance of wireless power transfer," *IEEE Trans. Power Electron.*, vol. 38, no. 6, pp. 6923–6928, Jun. 2023.
[22] H. Feng, T. Cai, S. Duan, X. Zhang, H. Hu, and J. Niu, "A dual-side-detuned series–series compensated resonant converter for wide charging region in a wireless power transfer system," *IEEE Trans. Ind. Electron.*, vol. 65, no. 3, pp. 2177–2188, Mar. 2018.
[23] S. Wu, C. Cai, A. Wang, Z. Qin, and S. Yang, "Design and implementation of a uniform power and stable efficiency wireless charging system for autonomous underwater vehicles," *IEEE Trans. Ind. Electron.*, vol. 70, no. 6, pp. 5674–5684, Jun. 2023.
[24] Y. Chen et al., "A clamp circuit-based inductive power transfer system with reconfigurable rectifier tolerating extensive coupling variations," *IEEE Trans. Power Electron.*, vol. 39, no. 2, pp. 1942–1946, Feb. 2024.
[25] H. Feng, A. Dayerizadeh, and S. M. Lukic, "A coupling-insensitive X-type IPT system for high position tolerance," *IEEE Trans. Ind. Electron.*, vol. 68, no. 8, pp. 6917–6926, Aug. 2021.
[26] M. Xiong et al., "Dual discrete-frequency reconfigurable IPT system with high misalignment tolerance for stable power transfer over extended coupling variation," *IEEE Trans. Power Electron.*, vol. 41, no. 3, pp. 4340–4350, Mar. 2026.
[27] Y. Chen et al., "Reconfigurable topology for IPT system maintaining stable transmission power over large coupling variation," *IEEE Trans. Power Electron.*, vol. 35, no. 5, pp. 4915–4924, May 2020.
[28] W. Zhao, X. Qu, J. Lian, and C. K. Tse, "A family of hybrid IPT couplers with high tolerance to pad misalignment," *IEEE Trans. Power Electron.*, vol. 37, no. 3, pp. 3617–3625, Mar. 2022.
[29] C. Chen, C. Q. Jiang, T. Ma, X. Wang, Y. Fan, and J. Xiang, "Misalignment tolerance extension for inductive power transfer system by utilizing slight frequency-detuned compensation," *IEEE Trans. Transp. Electrific.*, vol. 10, no. 4, pp. 9748–9760, Dec. 2024.
[30] B. Yang et al., "A detuned S-S compensated IPT system with two discrete frequencies for maintaining stable power transfer versus wide coupling variation," *IEEE Trans. Transp. Electrific.*, vol. 9, no. 3, pp. 3836–3848, Sep. 2023.

Chen Chen received the B.Eng. and M.Eng. degrees in mechanical manufacture and automation from the Wuhan University of Technology, Wuhan, China, in 2019 and 2022, respectively. He is currently working toward the Ph.D. degree with the Department of Electrical Engineering, City University of Hong Kong, Hong Kong SAR, China.

His research interests include wireless power transfer, and nanocrystalline material in power electronics.

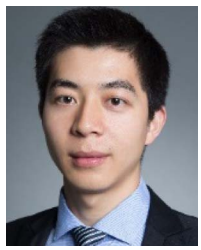

Chaoqiang Jiang (Senior Member, IEEE) received the B.Eng. and M.Eng. degrees in electrical engineering and automation from Wuhan University, Wuhan, China, in 2012 and 2015, respectively, and the Ph.D. degree in electrical and electronic engineering from The University of Hong Kong, Hong Kong SAR, China, in 2019.

He is currently an Associate Professor with the Department of Electrical Engineering and a faculty member with the State Key Laboratory of Terahertz and Millimeter Waves, City University of Hong Kong, Hong Kong SAR, China. From 2019 to 2021, he was a Postdoctoral Research Associate with the University of Cambridge, U.K. Also, he is affiliated with Clare Hall, University of Cambridge, Cambridge, since 2021. His research interests include power electronics, wireless power transfer, electric machines and drives, and electric vehicle (EV) technologies.

Dr. Jiang was the recipient of CENG Research Excellence Award, gold medal at the Silicon Valley International Invention Festival, gold medals with Congratulations of the Jury in International Exhibition of Inventions of Geneva, CAPE Acorn Blue Sky Research Award at the University of Cambridge, gold medal in 3rd Asia Exhibition of Innovations and Inventions, and first prize in the Interdisciplinary Research Competition at the University of Hong Kong. He is currently an Associate Editor of *IET Renewable Power Generation*, Guest Editor of IEEE OPEN JOURNAL OF VEHICULAR TECHNOLOGY, and IEEE TRANSACTIONS ON POWER ELECTRONICS (TPEL) Letters.

Fengshuo Yang received the B.S. degree in instrumentation science and engineering from the Harbin Institute of Technology, Harbin, China, in 2021, where he is currently working toward the Ph.D. degree in electrical engineering with the School of Electrical Engineering and Automation.

His research interests focus on wireless power transfer technology, particularly for applications in UAVs and AUVs.

Hao Guo received the B.S. degree in renewable energy science and engineering from Hohai University, Nanjing, China, in 2021, and the M.S. degree in electrical engineering from Southeast University, Nanjing, in 2024. He is currently working toward the Ph.D. degree in electrical engineering with the City University of Hong Kong, Hong Kong SAR, China.

His research interests include high-voltage direct current (HVdc) transmission systems, dc power flow controllers, and wireless power transfer (WPT) technologies.

Yue Liu was born in Jiangsu Province, China, in 1997. He received the B.S. and the Ph.D. degrees in electrical engineering from Nanjing University of Aeronautics and Astronautics (NUAA), Nanjing, China, in 2019 and 2024, respectively.

Since 2024, he has been a Postdoctoral Fellow with the Department of Electrical Engineering, City University of Hong Kong, Hong Kong. His main research interests include wide-bandgap devices, planar magnetic design, modeling and integration in power supplies, high-frequency power converters, resonant converters, and advanced power electronics architectures.

Ben Zhang received the Ph.D. in power engineering and engineering thermal physics from Harbin Engineering University, Harbin, China, in 2025.

He is a Postdoctoral Fellow with the Department of Electrical Engineering, the City University of Hong Kong, as well as a member of the State Key Laboratory of Terahertz and Millimeter Waves, since March 2025. His research interest includes WPT magnetic coupler design, WPT system control methodology studies, and the application of WPT systems in seawater environments.